TELKOMNIKA Telecommunication Computing Electronics and Control
Vol. 24, No. 5, October 2026, pp. 1728~1744
ISSN: 1693-6930, DOI: 10.12928/TELKOMNIKA.v24i5.27976

MRI segmentation and classification using 1-D and 2-D empirical mode decomposition

Giang Hong Nguyen[1,2], Yen Thi Hoang Hua[1], Ngan Vuong Thuy Nguyen[1], Liet Van Dang[3]
[1]Department of Physics and Computer Science, Faculty of Physics and Engineering Physics, University of Science, Viet Nam National University, Ho Chi Minh City, Vietnam
[2]Department of General Education, Cao Thang Technical College, Ho Chi Minh City, Vietnam
[3]Department of Nature, Dong Nai University, Tam Hiep Ward, Dong Nai City, Vietnam

Article Info

Article history:

Received Apr 1, 2026
Revised Jul 22, 2026
Accepted Aug 28, 2026

Keywords:

Bidimensional empirical mode decomposition
Bidimensional intrinsic mode function
Empirical mode decomposition
Empirical wavelet transform
VGG19-layer model

ABSTRACT

This study proposes a new framework for brain magnetic resonance imaging (MRI) tumor detection and classification using 1-D and 2-D empirical mode decomposition (EMD) / bidimensional empirical mode decomposition (BEMD). These adaptive algorithms optimize image denoising, segmentation and feature extraction. Tumors are detected using a global threshold derived from EMD-generated bimodal curves. A visual geometry group 19 (VGG19) model extracts features from the regions of interest (ROI) across both denoised images and BEMD components. The method was validated on the public Figshare brain tumor dataset. For segmentation, the proposed method performed similarly to multilevel Otsu, Kapur-Harmonic, and K-means algorithms. It achieved an average precision of 96.70%, slightly trailing K-means of 97.07%, and a sensitivity of 91.07%, outperforming K-means but falling behind Kapur and Otsu. Notably, it achieved the highest F1-score of 93.70%, tying the Otsu technique. These results highlight enhanced tumor localization, reflecting segmentation that closely aligns with the ground truth. For tumor classification, ensemble learning was used to develop nine models, all of which surpassed 93% accuracy; one achieved 100%, and three reached 96.7%. The proposed method outperformed seven state-of-the-art techniques with a peak accuracy of 99.02%, demonstrating its clinical viability. Overall, integrating EMD and BEMD algorithms provides a superior framework for brain tumor segmentation and classification compared traditional methods.

Corresponding Author:

Giang Hong Nguyen
Department of General Education, Cao Thang Technical College, Ho Chi Minh City
65 Huynh Thuc Khang, Sai Gon Ward, Ho Chi Minh City, Vietnam
Email: nguyenhonggiang@caothang.edu.vn; 22n38101@student.hcmus.edu.vn

1. INTRODUCTION

The brain is a vital but complex organ containing approximately 86 billion neurons, controlling voluntary and involuntary functions through the somatic and autonomic nervous systems. Brain injuries are classified as traumatic or non-traumatic, with brain tumors representing a major medical concern. The Global Cancer Observatory (GLOBOCAN) 2022 report indicated about 321,731 global brain tumor cases, resulting in 248,500 deaths, mainly in Asia [1]. Early detection significantly improves patient outcomes, but the skull structure makes diagnosis challenging. Non-invasive imaging techniques, particularly magnetic resonance imaging (MRI), play an important role because they provide safe and high-resolution images [2]. Accurate MRI interpretation depends on radiologist expertise and image quality. To improve diagnostic accuracy, computer-aided diagnosis (CADx) systems have been developed. These systems typically include

preprocessing, segmentation, and classification using traditional machine learning (ML) or deep learning (DL) methods. Preprocessing enhances image quality and removes artifacts to ensure accuracy in subsequent stages. Segmentation then isolates the tumor to reveal its geometry and location, while classification categorizes it as benign, malignant, or indicative of a specific disease. Two final stages enhance automated workflows by reducing diagnostic errors, accelerating clinical assessments, and improving patient outcomes [3], [4]. The challenge of working is to develop methods that are both accurate and practical to maximize their clinical utility. Currently, research in CADx systems heavily emphasizes deep learning. However, the need for large, labeled datasets and high computational power often restricts its application in developing regions. Consequently, traditional and hybrid techniques for segmentation and classification remain highly relevant. However, when applied to brain MRI, they face challenges such as noise, intensity variations, and anatomical complexity. These issues lead to three key limitations: (i) global thresholding is often insufficient for detecting tumors; (ii) multilevel thresholding requires a trial-and-error approach to determine optimal thresholds; and (iii) features extracted from denoised regions of interest (ROIs) may overlook subtle clinical details. To address these limitations, this paper proposes a novel framework using empirical mode decomposition (EMD, 1-D) and bidimensional empirical mode decomposition (BEMD, 2-D) for signal and image processing. These adaptive, multiresolution, data-driven techniques decompose complex non-linear and non-stationary data into intrinsic mode functions (IMFs) and bidimensional intrinsic mode functions (BIMFs) through a "sifting process" without relying on fixed basis functions. Because each IMF and BIMF represent oscillations at distinct frequencies, this process significantly enhances the capture of structural and textural details across different scales, improving overall analysis. This study introduces a tumor detection approach that integrates the empirical wavelet transform (EWT) and EMD, while using BEMD alongside visual geometry group 19 (VGG19) for feature extraction. The following section reviews prior work on traditional and hybrid segmentation and classification methods.

Shemanto *et al*. [5] developed HOFilter for MRI tumor detection, utilizing a median filter (applied five times) and a global 255-scale Otsu threshold. The threshold is divided into four incremental groups, producing 94.46% accuracy on 198 Kaggle dataset MRIs. However, the exact criteria for the added threshold values remain unexplained. Sharma *et al*. [6] proposed a hybrid multilevel thresholding technique powered by the dynamic opposite bald eagle search algorithm. This method uses Kapur's entropy to determine optimal threshold values. Tested on MRIs from the Figshare dataset for tumor detection, the proposed approach demonstrated superior performance over the Bald Eagle Search and multiple other multilevel thresholding techniques. Akan *et al*. [7] proposed a hybrid three-dimensional (3D) segmentation method using histogram smoothing, multimodal particle swarm optimization, and non-Euclidean pixel clustering. Evaluated on three datasets, the model achieved 95.52% accuracy and 85.15% recall. Krinidis *et al*. [8] proposed determining the global image threshold using the EMD of the probability mass function (PMF). They constructed a thresholding curve by summing the IMFs, excluding the first and last. However, this method is limited to single-peaked distributions and cannot support multilevel thresholding. Rao and Reddy [9] adapted this curve-building approach, although it lacks clear peak and valley definitions. To determine the number of clusters and initial centers for fuzzy C-means segmentation, they applied a double-cut technique; however, this approach demands high computational resources.

Lakshmi *et al*. [10] used bilateral filtering and MEDU-Net+ for noise removal and semantic segmentation in brain MRI analysis. They used ResNet50 for feature extraction and a Bayesian regularized ML technique, brain, for tumor assessment. After fine-tuning brain's parameters, their methodology classified MRI images from the Kaggle dataset into three tumor types and one non-tumor type, achieving an accuracy of 97.75% after 1000 epochs. Aamir *et al*. [11] proposed a hybrid brain tumor classification framework using anisotropic Gaussian denoising, morphological enhancement, U-Net region of interest (ROI) extraction, and multiscale DenseNet feature extraction. The classification used random forest (RF), support vector machine (SVM), and K-nearest neighbors (KNN) models, achieving accuracies of 99.67% on the Fishare dataset and 99.94% on Kaggle. Kumar *et al*. [12] improved brain MRI classification by integrating image enhancement with EWT. By extracting energy and entropy features from EWT subbands, they built robust feature vectors to train SVM and LPBoost classifiers. Evaluated on 280 images, both SVM (using Littlewood-Paley-based EWT) and LPBoost (using tensor-based EWT) achieved an accuracy of 96.43%. Gudigar *et al*. [13] conducted a review on Decomposition Techniques in MRI analysis, comparing BEMD and variational mode decomposition (VMD) for classification. They classified the data using bispectral features, supervised neighborhood projection embedding, and an SVM classifier. VMD achieved a multi-class accuracy of 90.68%, outperforming BEMD's 84.47%. However, specific details on feature extraction components are lacking. Additionally, Sahu *et al*. [14], Deb *et al*. [15], and Ghazi *et al*. [16] used BEMD to classify MRI, esophageal images, and mammography images, respectively. This will be discussed in further detail in comparison with existing 2D-EMD approaches. By exploring BEMD for feature extraction, the latest three studies offer critical perspectives on modern signal and image processing.

The papers in the literature review confirm the stated limits of traditional and hybrid methods. This study aims to address these limitations. Our key contributions include: (i) developing an MRI tumor segmentation framework that uses EWT and EMD for global threshold detection; (ii) high-level features are extracted by VGG19 from a combination of the ROIs from denoised images and the BIMFs via BEMD; and (iii) designing high-performing, multi-class classification models using ensemble bagging and boosting methods. These contributions aim to deliver a robust CADx system that minimizes diagnostic misclassification, establishing a strong foundation for clinical deployment.

The remainder of this paper is structured as follows. Section 2 describes the data, equipment, and methodology. Section 3 presents experimental results and discussion. Section 4 provides conclusions and future work.

2. METHOD

2.1. Data and equipment

The Figshare brain tumor dataset consists of 3,064 T1-weighted contrast-enhanced MRIs from 233 patients, collected at Nanfang Hospital and Tianjin Medical University in China between 2005 and 2010. Each 512×512 image features an in-plane resolution of 0.49×0.49 mm^2. The collection includes 1,426 gliomas, 930 pituitary tumors, and 706 meningiomas, and provides tumor labels, patient IDs, original images, and mask data [17], [18]. For our experiments, nine images were selected for segmentation, and 150 images (50 per tumor type) were used for classification. Prior to segmentation and feature extraction, all images were enhanced. All experiments were conducted in MATLAB on a laptop equipped with an Intel Core i5 processor and 8 GB RAM, using Thirumalaisamy's fast and adaptive BEMD code [19] and anisotropic diffusion filtering (ADF) code [20].

2.2. Methods

2.2.1. Background theories

The introduction provided a brief overview of EMD and BEMD. These algorithms convert a signal or an image into IMFs or BIMFs, with each IMF and BIMF satisfying criteria: (i) the number of extrema and zero crossings must either be equal or differ by at most one; and (ii) the mean value of the upper and lower envelopes must be zero. The EMD algorithm operates through two loops: the inner loop determines individual IMFs using a "sifting process", which involves identifying local maxima and minima, constructing upper and lower envelopes, and iteratively subtracting the mean until the IMF conditions are satisfied, while the outer loop extracts successive IMFs and the final residue. The BEMD algorithm is an extension of EMD to two dimensions. However, while EMD uses 1-D envelope interpolation, BEMD uses surface interpolation [21]. Algorithm 1 shows the EMD algorithm.

Algorithm 1. EMD algorithm (note: criteria of IMF (i) and (ii) in text)

Step 1: Initialization
Set input S(x)
Set $r_0 = S(x)$
j = 1 (index of IMF)

Step 2: Inner loop (Sifting process - Single IMF)
$d_0 = r_{j-1}(x)$
$m = 1$

(i) Find local extreme: local extreme in $d_{m-1}(x)$

(ii) Building envelopes: upper and lower envelopes:
- Interpolating local extreme by cubic spline, $u_{max}(x)\ and\ u_{min}(x)$

(iii) Computing mean envelopes:
$$av_{m-1}(x) = \frac{[u_{max}(x)+u_{min}(x)]}{2}$$

iv) Oscillation component:
$$d_m(x) = d_{m-1}(x) - av_{m-1}(x)$$

(v) Stop condition of sifting process:
- if : $d_m(x) == Criteria$: False
  $d_{m-1}(x) = d_m(x)$
  $m = m + 1$ repeat Step 2(i)
- if : $d_m(x) == Criteria$: True (obtain IMF)
  goto Step 3

Step 3: Outer loop (Multiple IMFs and Residue)

(i) Store IMF:
$IMF_j(x) = d_m(x)$

(ii) Update residue:
$r_j(x) = r_{j-1}(x) - IMF_j(x)$

```
(iii) Stop condition:
      - if r_j(x): multiple extreme
              Set j = j + 1 go to Step 2
      - if r_j(x): monotonic trend:  Res = r_j(x)
                    Algorithm stop
```

Finally, the input data is modeled by (1) and (2):

– For EMD:

$$S(x) = \sum_{i=1}^{n} IMF_i(x) + Res_n(x) \quad (1)$$

where, $S(x)$: the input signal, $IMF_i(x)$: the i_{th} IMF and $Res_n(x)$: the final residue.

– For BEMD:

$$I(x,y) = \sum_{i=1}^{n} BIMF_i(x,y) + RES_n(x,y) \quad (2)$$

where, $I(x,y)$: the input image, $BIMF_i(x,y)$: the i^{th} BIMFs and $RES_n(x,y)$: the final residue.

IMFs and BIMFs represent oscillatory components ranging from high to low frequencies, corresponding to short-term (fine texture) and long-term (larger structural changes) variations, while the final residue (RES) reflects the overall trend of the signal or the background of the image.

EWT combines principles of wavelet transform and EMD to identify frequency supports in the Fourier spectrum and construct adaptive wavelet filters. Unlike EMD, which relies on temporal extrema, EWT analyzes the signal in the frequency domain. It involves four steps: (i) performing fast fourier transform (FFT) for magnitude spectrum analysis, (ii) segmenting the spectrum by detecting significant spectral peaks, (iii) constructing band-pass filters using Littlewood–Paley functions, and (iv*)* applying the filters to extract empirical modes [22].

$$s(x) = W_s(0,x)\ X\ \emptyset_1(x) + \sum_{i=1}^{N} W_s(i,x)\ X\ \psi_i(x) \quad (3)$$

where, $s(x)$: the input, X: inner product, $\emptyset_1(x)$: the scaling function, $\psi_i(x)$: the empirical wavelet functions, and W_s: the corresponding transform coefficients.

EWT decomposes a signal into two components: an approximate component (cA) and a detailed component (cD). Processing can be performed on one or both components depending on the intended result. The diagram of the EWT algorithm is shown in Figure 1.

Figure 1. Diagram of the EWT

2.2.2. Proposed method

The proposed approach uses EMD and BEMD, because they are data-driven methods, their resulting components IMFs and BIMFs are data-adaptive, created directly from local data features based on varying frequencies; these components reveal hidden textures in the data at different scales [23]. Therefore, specific features can be selected, making them highly useful for analyzing complex images, particularly medical images. Structurally, the proposed methodology is executed through three main stages: image enhancement, segmentation, and classification.

Image enhancement is performed in three steps; (i) skull stripping: crop 3–4 pixels from the image borders to remove the light box, then apply thresholding and morphological operators to strip the skull [24]; (ii) noise reduction: the image is processed using BEMD and an anisotropic diffusion filter; and (iii) contrast enhancement: top-hat and bottom-hat morphological transforms are used. Finally, wavelet fusion integrates the results of steps (ii) and (iii) [25].

An image histogram represents the frequency distribution of pixel intensities. The PMF is defined as [8]:

$$PMF(k) = \frac{h(k)}{M \times N} \quad (4)$$

where, $h(k)$: the histogram, (MxN): the total number of pixels in the image; for an 8-bit grayscale image, $k \in [0,255]$.

The PMF reflects background, objects, and boundaries through its peaks and valleys. However, determining the threshold directly from $PMF(k)$ is difficult due to noise and high-frequency pixels. The proposed approach includes: (i) computing the PMF from the histogram; (ii) smoothing the PMF: EWT decomposes the PMF into approximation (cA) and detail (cD) components. Discarding the detail-heavy, noisy cD component while retaining the low-frequency cA component yields a smoothed PMF for the next step; (iii) constructing a threshold curve: decomposing the smooth approximation cA via EMD yields several IMFs and a residue. Since cA is smooth, the highest-frequency component IMF_1 is virtually noise-free and clearly isolates two distinct modes: one corresponding to brain structure and another to tumor presence. Consequently, IMF_1 is selected as the threshold curve PMF_{Th} for determining the global threshold; and (iv) tumor detection: the threshold from the PMF_{Th} curve, defined as the pixel value at the minimum valley between the two peaks, is used to binarize the denoised MRI for raw tumor detection. Subsequently, morphological operators are applied to refine the segmentation.

Following segmentation, the tumor center is identified, and a ROI measuring 224×224 pixels is extracted around the tumor in the enhanced MRI, then BEMD is applied to the ROI to generate BIMFs: (i) feature extraction: the ROIs of two specific BIMFs are selected and integrated with the enhanced MRI's ROI to create a red-green-blue (RGB) image with enhanced feature inputs. Finally, high-level features are extracted from this integrated RGB image and MRI's ROI using the fc7 layer of a pre-trained VGG19 model, generating 4096 features per MRI scan; and (ii) classification: the dataset is standardized and split into training and testing subsets at an 80:20 ratio. Finally, ensemble learning techniques are applied, integrating parallel base model training via bagging with sequential error correction through boosting [26]–[28].

Tumor detection and classification results are evaluated against the dataset's ground truth, using the following standard performance metrics such as accuracy, precision, sensitivity, specificity, and F1-score [29]:

$$Accuracy = \frac{TP+TN}{TP+TN+FP+FN} \quad (5)$$

$$Precision = \frac{TP}{TP+FP} \quad (6)$$

$$Sensitivity = \frac{TP}{TP+FN} \quad (7)$$

$$Specificity = \frac{TN}{TN+FP} \quad (8)$$

$$F_1 - score = 2.\frac{Precision*Sensitivity}{Precision+Sensitivity} \quad (9)$$

where, TP: true positive, TN: true negative, FP: false positive and FN: false negative.
The flow diagram of the proposed approach is illustrated in Figure 2.

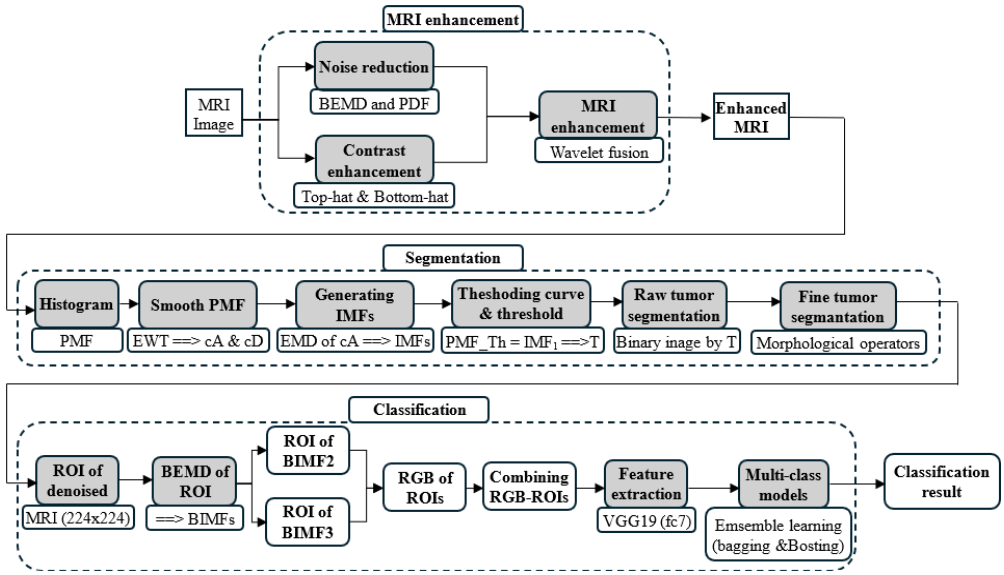

Figure 2. The flow diagram of the proposed approach

3. RESULT

3.1. Tumor detection

This section presents tumor detection results for nine MRI images across three tumor types, beginning with the processing steps for MRI-2315. Steps for tumor detection of MRI-2315:

– Image enhancement and $PMF(k)$ curve

Figure 3(a) presents MRI-2315 (glioma), which was initially skull-stripped [24]. Its quality was then enhanced using BEMD and ADF for noise reduction and morphological contrast enhancement [25], as illustrated in Figure 3(b). The $PMF(k)$ depicted in Figure 3(c) displays indistinct valleys that complicate threshold selection. Consequently, this curve is used to construct the thresholding curve.

– Smoothing $PMF(k)$ using EWT

The EWT decomposes the $PMF(k)$ into two parts: a high-frequency detail component (cD) (Figure 3(d), solid line) containing noise and fine details, which is discarded and a low-frequency approximation component (cA). This preserves the main structure of $PMF(k)$ while reducing noise, resulting in a smoothed $PMF(k)$ illustrated by the solid line in Figure 3(e), whereas the original $PMF(k)$ appears as a dashed line.

– Building a threshold curve using EMD

Figure 3(f) shows the decomposition of the smoothed $PMF(k)$ (cA) into IMFs and a residue (RES) using EMD. IMFs represent oscillations at different frequencies from high to low, and the RES indicates the trend. Due to the denoising and smoothing input, then IMF_1, the highest-frequency component, becomes noise-free and forms a bimodal curve, making it suitable for threshold detection.

$$PMF_{Th}(k) = IMF_1(k) \tag{10}$$

Figure 3(g) illustrates the $PMF_{Th}(k)$ curve, which contains two peaks corresponding to brain tissue and tumor regions. The threshold $T = 81$ is determined at the minimum valley between the two peaks. Similarly, Figure 3(h) shows the $PMF_{Th}(k)$ curve from the Krinidis technique [8]. This approach sums multiple IMFs (from IMF_2 to IMF_{max-1}) via EMD to build a thresholding curve with $T_1 = 80$. Although the thresholds of the two methods are considered equal, Krinidis's curve exhibits a sub-peak, and the IMF summation limits its adaptability to multilevel thresholding [9]. Conversely, the proposed method integrates EWT and IMF using only IMF_1, generating a clear, bimodal curve without sub-peaks. Once detrended, it produces a multimodal curve that facilitates finding multilevel thresholds for brain tissue and tumor layer analysis.

– Tumor detection and comparison

This threshold identifies the raw tumor detection, overlaid on the original MRI in Figure 3(i) (1). Figure 3(i) (2-5) presents a comparison of the proposed method's results against three reference techniques: Otsu's multilevel threshold [30], Kapur's method with optimal harmonic search [31], and K-means clustering [32]. Color coding indicates: detected tumors (white), differences (gray), and ground truth (green curve). Post-processing uses consistent morphological operations. Visual assessment indicates that the Otsu method closely matches the ground truth, followed by the proposed approach and Kapur's method, and finally K-means. Performance metrics are summarized in Table 1.

3.1.1. Tumor detection for the remaining eight MRIs

Figure 4 illustrates the tumor detection results for eight selected MRI images, comparing the proposed technique against three reference methods. Specifically, Figure 4(a) shows the skull-stripped and enhanced MRI, while Figure 4(b) presents the $PMF(k)$ curve (dash-line) alongside its smoothed version (solid line). Figure 4(c) details the bimodal curve $PMF_{Th}(k)$ derived from $IMF_1(k)$ using EMD which establishes the threshold. Figure 4(d) (1) presents the raw detected tumor highlighted in red on the original MRI. Figures 4(d) (2–5) depict the refined tumors generated by the proposed algorithm and the three comparison methods. Visual evaluation indicates that the Otsu method aligns most closely with the ground truth, followed by the proposed approach, Kapur's method, and K-means, respectively. Within the glioma group, images 2407 and 2730 particularly image 2407 displayed the largest discrepancies between the detected tumors and the ground truth compared to other groups. Detailed performance metrics are summarized in Table 1.

3.1.2. Performance metrics

In MRI scans, brain tumors are typically much smaller than the surrounding tissues, causing true negative (TN) values to dominate and inflate both accuracy and specificity to near 1. To avoid these misleading results, detection performance is instead evaluated using precision, sensitivity, and the F1-score (Table 1). The average precision of the proposed approach reached 96.70%, which is slightly lower than the K-means method (97.07%). In terms of sensitivity, the proposed approach achieved 91.07% surpassing K-

means (89.27%) but trailing the Kapur and Otsu methods. Because the differences in precision and sensitivity between these methods are minor, both Otsu's method and the proposed approach both establish an optimal trade-off between the two metrics (ranking second and third). Conversely, the Kapur and K-means models lack this balance (ranking first and fourth, trade-off). As a result, the proposed approach shares the top-ranked F1-score with Otsu (93.70% vs. 93.71%). This demonstrates that both methods effectively balance the segmentation of detected tumors and ground truths, and minimize false detections [33].

The threshold values in column 4 of Table 1 indicate that the proposed approach is more consistent with Otsu's multilevel method than with the Kapur-Harmonic method. Although the proposed method is global, it provides thresholds comparable to the standard Otsu multilevel technique. This successfully bypasses the trial-and-error process typically required to determine the optimal threshold of multilevel thresholding, highlighting the practical effectiveness of the proposed approach.

Comparison with existing EMD approaches: the results were compared with those of the modified Krindinis thresholding method detailed in [34]. In that study, the authors summed from IMK_2 to IMF_{max-2} instead of IMF_2 to IMF_5 as Krindinis *et al.* did [8], evaluating their approach on nine MRI images from the Figshare dataset. While they reported an average precision of 80.12%, sensitivity of 98.4%, and F1-score of 88.85%, our approach achieved 96.70%, 91.07%, and 93.70%, respectively, demonstrating our method's overall superiority.

Computational time: the proposed approach achieved a runtime of approximately 1.71 seconds, ranking third among the four methods. It was faster than the Kapur-Harmonic search (~3.91 s), but slower than the Otsu (~0.25 s) and K-means (~0.24 s) methods, as detailed in the final column of Table 1.

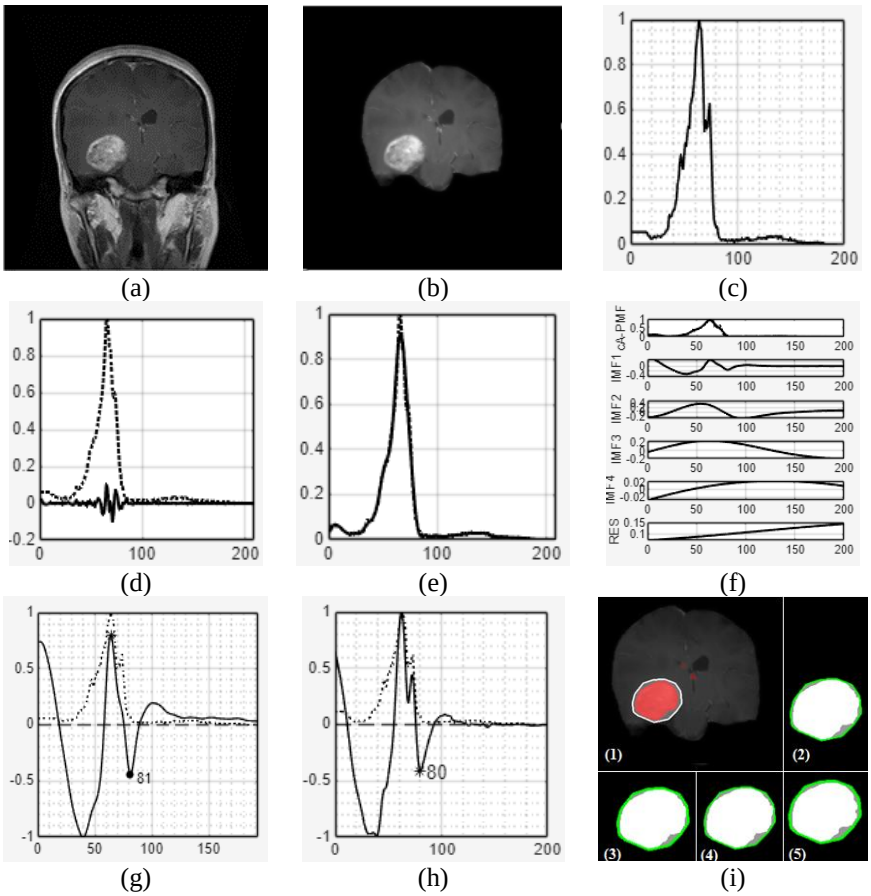

Figure 3. Tumor detection steps for MRI-2315: (a) original image, (b) denoised image, (c) $PMF(k)$ curve, (d) EWT detail component cD, (e) EWT approximation coefficient cA used as smoothed $PMF(k)$, (f) IMFs and residue using EMD, (g) $PMF_{Th}(k)$ curve of the proposed approach, (h) $PMF_{Th}(k)$ curve from Krinidis (for reference) [8], and (i) tumor detection results of the proposed method. Panels show: (1) raw tumor detection overlaid on the original image, and (2-5) refined tumor detection using: (2) the proposed approach, (3) Otsu's multilevel thresholding, (4) Kapur's multilevel thresholding, and (5) K-means clustering

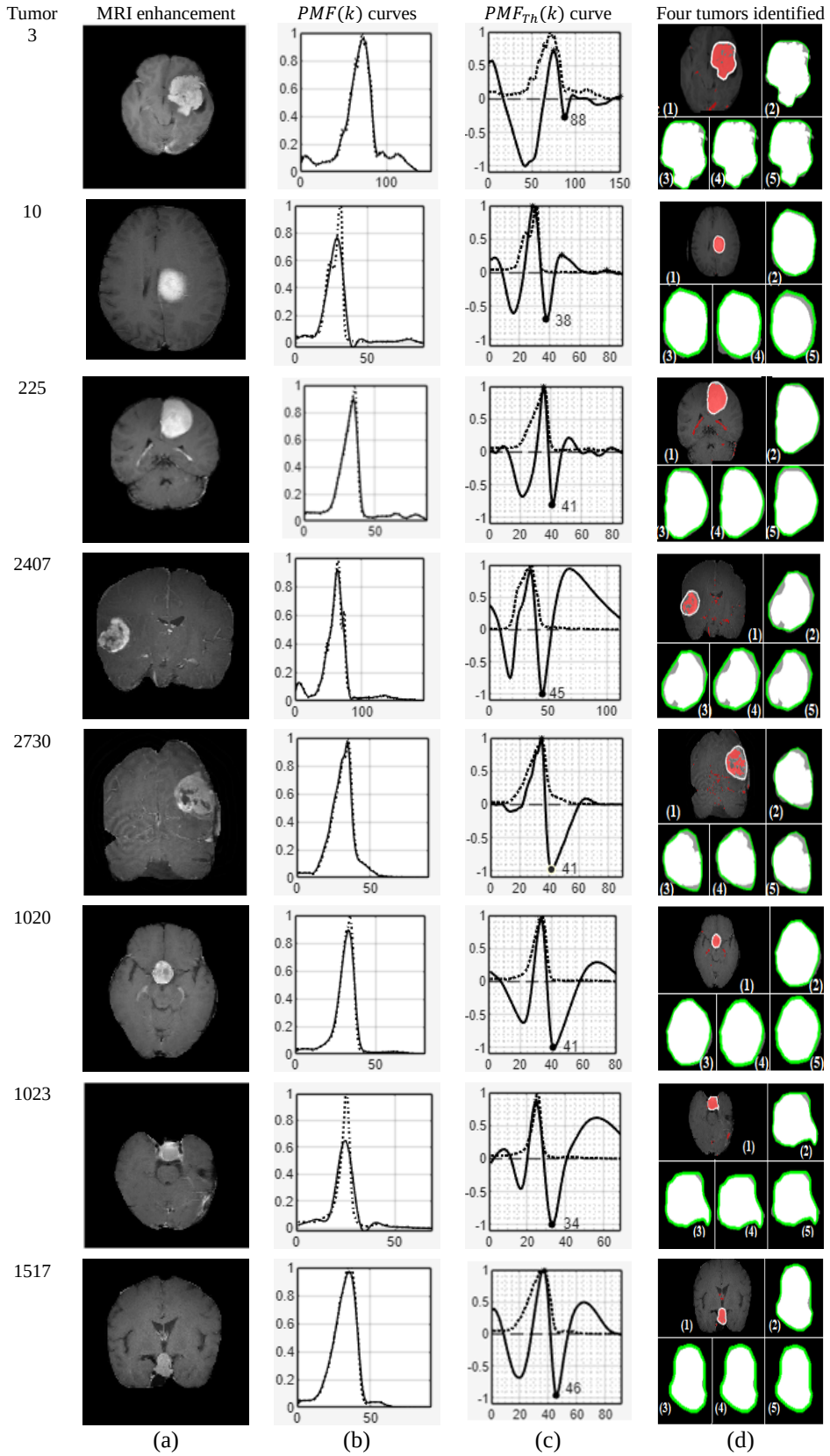

Figure 4. Results of the tumor detection process were obtained for the remaining eight MRI images: (a) MRI enhancement with skull stripping, (b) $PMF(k)$ curves and smoothed versions using EWT, (c) $PMF_{Th}(k)$ curve derived from $IMF_1(k)$ using EMD, and (d) tumor detection results. Panels show: (1) raw tumor detection overlaid on the original image, and (2-5) refined tumor detection using: (2) the proposed approach, (3) Otsu's multilevel thresholding, (4) Kapur's multilevel thresholding, and (5) K-means clustering

Table 1. The performance metrics for the four segmentation algorithms on nine MRIs

No	MRI	Method	Threshold	Pre. (%)	Sen. (%)	F1-Score (%)	Time (s)
Gliomas	2315	Proposed A.	**81**	99.96	87.51	93.32	1.73
		Multi-Otsu	23 57 **89** 129	99.92	88.28	93.74	0.27
		Kapur-Har.	**81** 194	99.96	87.51	93.32	2.80
		K-means	**3** Cluster	100	84.40	91.54	0.29
	2407	Proposed A.	**45**	97.72	79.95	87.95	1.41
		Multi-Otsu	12 30 **45** 68	97.72	79.95	87.95	0.24
		Kapur-Har.	**46** 113 184	97.81	79.33	87.60	3.97
		K-means	**3** clusters	97.99	78.75	87.32	0.26
	2730	Proposed A.	**41**	92.77	87.69	90.16	1.46
		Multi-Otsu	10 20 29 34 **42**	93.40	86.97	90.07	0.14
		Kapur-Har.	**40** 58 91 132 173 214	92.41	88.82	90.58	3.62
		K-means	**4** clusters	92.77	87.69	90.16	0.49
Meningiomas	3	Proposed A.	**88**	95.68	92.82	94.23	1.61
		Multi-Otsu	26 62 **90**	96.31	89.86	92.98	0.25
		Kapur-Har.	**85** 153	95.16	94.09	94.62	4.26
		K-means	**3** clusters	95.32	93.50	94.40	0.25
	10	Proposed A.	**38**	95.37	96.17	95.77	1.66
		Multi-Otsu	14 **37** 60	94.04	96.98	95.48	0.26
		Kapur-Har.	35 90 146 201	89.94	98.17	93.87	3.48
		K-means	**3** clusters	99.93	81.79	89.96	0.20
	225	Proposed A.	**41**	94.51	95.86	95.18	1.70
		Multi-Otsu	16 **43** 67	95.17	95.12	95.14	0.33
		Kapur-Har.	**40** 88 172	94.24	96.24	95.23	3.28
		K-means	**3** clusters	96.84	91.69	94.20	0.21
	1020	Proposed A.	**41**	96.51	95.38	95.94	2.20
		Multi-Otsu	16 **41** 59	96.51	95.38	95.94	0.17
		Kapur-Har.	**40** 82 169	95.19	96.94	96.06	3.36
		K-means	**3** clusters	95.74	95.39	95.56	0.61
Pituitary	1023	Proposed A.	**34**	98.50	91.83	95.05	1.52
		Multi-Otsu	12 22 **32** 47 60	97.45	93.54	95.45	0.23
		Kapur-Har.	**30** 70 116 163 209	94.70	95.27	94.98	3.15
		K-means	**3** cluster	97.78	93.09	95.38	0.36
	1517	Proposed A.	**46**	99.25	92.38	95.69	2.12
		Multi-Otsu	13 30 **44** 89	98.72	94.72	96.68	0.34
		Kapur-Har.	44 **93 134 174 215**	98.72	94.72	96.68	7.30
		K-means	**4** clusters	97.28	96.80	97.04	0.36
Average KPIs		Proposed A.		**96.70** (ii)	**91.07** (iii)	**93.70** (i)	**1.7122** (iii)
		Multi-Otsu		**96.58** (iii)	**91.20** (ii)	**93.71** (i)	**0.2478** (i)
		Kapur-Har.		**95.35** (iv)	**92.34** (i)	**93.66** (iii)	**3.9133** (iv)
		K-means		**97.07** (i)	**89.23** (iv)	**92.84** (iv)	**0.3367** (ii)

Notes: Roman numerals denote the order of the approaches according to each performance metric: (i) first, (ii) second, (iii) third, and (iv) fourth

Based on the presentations, considering both accuracy and computation time, the Otsu's method is the most efficient. However, when simplicity is also factored in, our proposed approach is the best. It achieves comparable accuracy without relying on the predefined criteria that the three reference methods must use.

3.2. Classification

Data preparation: because subtle features are often hidden deep within enhanced MRI scans, extracting them directly from the ROI often falls short. Therefore, BEMD is applied to the ROI to generate BIMFs; each BIMF contains instantaneous amplitude and frequency information, allowing the model to adapt to local image variations across different scales. In our classification, $BIMF_2$ and $BIMF_3$ were selected because they retain the texture details, edges, and structures dominating the mid-frequency range, while excluding both the noise ($BIMF_1$) and the trend (the last BIMFs). Figures 5(a) to (f) illustrates the enhanced MRI, ROI images, and their corresponding BIMF components and integrated ROI. Specifically, the images presented in Figures 5(b) and 5(f) were used for feature extraction.

Classification was performed using 150 ROI images from the brain MRI Figshare dataset. These images were processed using BEMD to extract high-to-mid frequency components ($BIMF_2$ and $BIMF_3$). Feature extraction inputs included the RGB-ROI images and combinations of the RGB-ROI with RGB-BIMFs. These inputs were analyzed using a pre-trained VGG19 model to extract high-level features from a fully connected fc layer, resulting in a feature vector of size 150×4096.

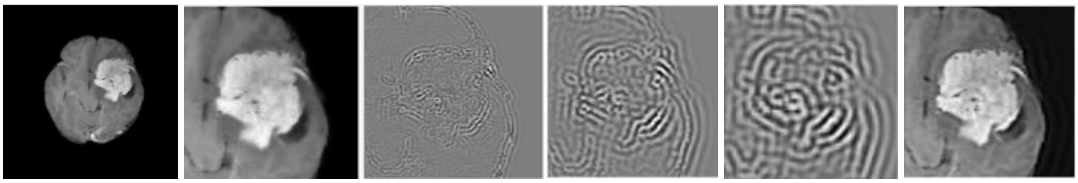

(a) (b) (c) (d) (e) (f)

Figure 5. Input MRI for VGG19 feature extraction: (a) enhanced MRI (512×512), (b) tumor ROI (224×224), (c) $BIMF_1$ of ROI with noise, (d) $BIMF_2$ of ROI (ROI_1), (e) $BIMF_3$ of ROI (ROI_2), and (f) RGB integrated ROI, ROI_1, and ROI_2. (note: Figure 5(b) and Figure 5(f) serve as inputs for feature extraction)

Feature extraction: a total of 150 enhanced images from the Figshare Brain MRI dataset were used for feature extraction. The ROIs were extracted and processed using BEMD to obtain the corresponding $BIMF_2$ and $BIMF_3$ components. The input for feature extraction was divided into two groups: (i) RGB-MRI's ROIs and (ii) a combined image of RGB-MRI's ROIs and RGB-$BIMF_k$'s ROIs ($k = 2, 3$). A pre-trained VGG19 model was used to extract high-level features from the fully connected fc7 layer, generating a feature vector of size 150×4096 for each data group.

Classification: the dataset was randomly divided into an 80:20 ratio for the training and test sets, and subsequently fed into MATLAB's fit ensemble function to create a classification model [35]. The ensemble learning process optimizes predictive performance by balancing bias and variance. It achieves this by aggregating base learners through bagging techniques (such as standard bagging and random Subspace/SubBoost) and sequential boosting algorithms (including TotalBoost, AdaBoost, LPBoost, and RUSBoost). The resulting model classifies the data into three distinct disease categories: gliomas, meningiomas, and pituitary tumors; achieving an accuracy of at least 93% on both the training and test sets.

3.2.1. Results

This section details the best-performing classification models across the two image modalities used for feature extraction.

a. Case study I - feature extraction using VGG19 with RGB-ROI

In this case, features were extracted directly from RGB-ROI images and standardized for ensemble learning, producing four high-accuracy models with distinct base learners. Boosting models were executed every 1,000 cycles. Figure 6 presents the confusion matrices for these models, with Figure 6(a) demonstrating a perfect 100% training accuracy across all four.

SubBoost model using KNN ($k = 5$), allowed for joint multivariable updates. This statistical technique was highly efficient for high-dimensional datasets where the feature size exceeded the sample size, as in this study; it resampled data at the start of each iteration [36]. This model achieved 100% accuracy on the training set. Evaluation on the test set produced 96.7% accuracy (with a single meningioma misclassified as a pituitary tumor), 96.3% precision, 97.79% sensitivity, and a 96.5% F1-score (Figure 6(b)). These robust metrics highlighted the model's viability for clinical application.

AdaBoost, LPBoost, and bagging used decision trees (DT) as base learners due to their highly suitable structures for assembling. While all three models achieved 100% accuracy on the training set (Figure 6(a)), their test set accuracy was 93.3% (with each yielding 2 misclassifications out of 30) (Figures 6(c)-(e)), which was lower than that of the SubBoost model. This performance gap occurred because AdaBoost and LPBoost used all features during each iteration, meaning noisy features could negatively impact model outcomes [37]. Meanwhile, unlike SubBoost, which applied resampling iteratively, bagging resampled subsets of the dataset simultaneously, trained a separate model on each subset in parallel, and focused on reducing variance. Therefore, it typically produced lower accuracy than SubBoost [36], [37]. Nevertheless, with precision, sensitivity, and F1-scores ranging from 93.3% to 94.2%, these models demonstrated a strong ability to avoid misclassification errors. The training times for model construction ordered from fastest to slowest were bagging (1.8 s), subSpacet (2 s), LPBoost (17 s), and AdaBoost (553.6 s). Consequently, considering both computational efficiency and classification accuracy, subSpace emerged as the optimal model.

b. Case study II- feature extraction using using VGG19 with a combined RGB-ROI, RGB-$BIMF_2$ and RGB-$BIMF_3$

In this case, features were extracted from the RGB-ROI combined with RGB-$BIMF_2$ and RGB-$BIMF_3$. This combination captured subtle information that might have been missed by using the RGB-ROI alone. Prior to model training, the extracted features were standardized to ensure consistent scaling, and an ensemble learning approach with 1,000 boosting cycles was applied. The results indicated that the bagging,

AdaBoost, LPBoost, and TotalBoost models achieved 100% training accuracy (Figure 7(a)), while RUSBoost achieved 98.3% training accuracy (Figure 7(b)).

The bagging model used DT with a minimum leaf size of one, allowing them to grow completely until every leaf contained exactly one training sample. This unrestricted growth caused individual trees to perfectly memorize the training data. However, bagging which averages the predictions of multiple trees effectively canceled out individual errors and reduced model variance [36], [38], making it well-suited for the small dataset used in this study. Therefore, unsurprisingly, this ensemble approach produced 100% accuracy on both the training and test sets. The corresponding confusion matrix is shown in Figure 7(a).

AdaBoost, LPBoost, and TotalBoost models: these models used DT with surrogate split methods and six branch nodes. Surrogate splits improved the DT robustness against noise, stabilized accuracy, and mitigated overfitting. Additionally, limiting the trees to six nodes allowed the models to effectively manage missing data and outliers [39], [40]. All three models achieved 100% training accuracy but produced varying test results. The AdaBoost model achieved 96.7% accuracy with one misclassification (gliomas classified as meningiomas) (Figure 7(c)). Although both LPBoost and TotalBoost were capable of self-adjustment and self-termination [41], minor discrepancies in their predictive accuracies existed due to distinct approaches in handling optimization and data redundancy. Specifically, LPBoost achieved 96.7% accuracy with one misclassification (meningiomas classified as gliomas) (Figure 7(d)), and TotalBoost achieved 93.3% accuracy with two misclassifications (gliomas and pituitary classified as meningiomas) (Figure 7(e)).

The RUSBoost model used pseudo-linear discriminants as its base learners, facilitating oblique decision boundaries that separated complex classes more effectively. This capability was particularly advantageous for small datasets, enabling rapid and accurate model construction [42]. However, because the model balanced the dataset by under sampling the majority class during each iteration, a corresponding decrease occurred in majority class accuracy. Consequently, the model achieved an overall accuracy of 98.3% on the training set (Figure 7(b)) and 93.3% on the testing set (Figure 7(f)), while other performance metrics remained unaffected.

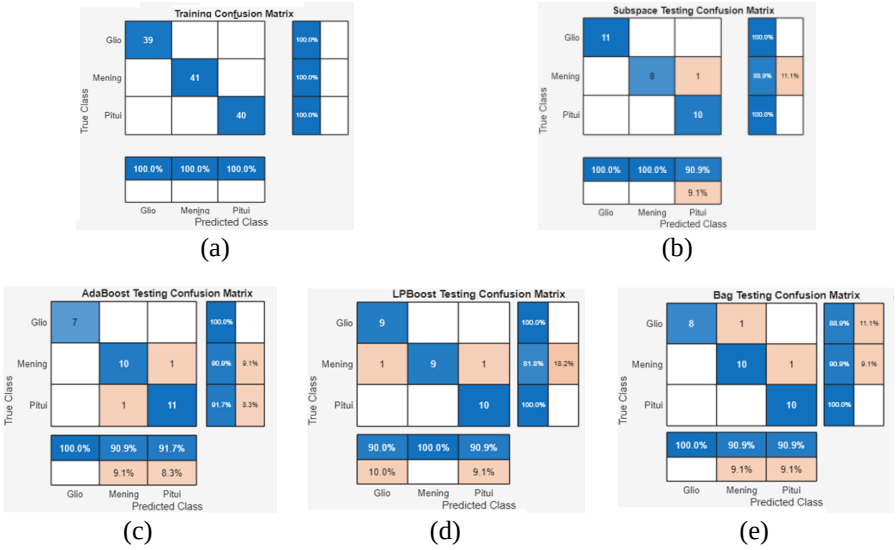

Figure 6. Confusion matrix of four models in case study I; (a) the confusion matrix for the training set of four models: SubBoost, AdaBoost, LPBoost, and bagging (100% accuracy), (b) the test set confusion matrix of SubBoost model (96.7% accuracy), (c) the test set confusion matrix of AdaBoost (93.3% accuracy); (d) the test set confusion matrix of LPBoost (93.3% accuracy); and (e) the test set confusion matrix of bagging (93.3% accuracy)

The confusion matrices (Figure 7) demonstrated that the models achieved high performance across all evaluation metrics, with precision ranging from 92.6% to 100%, sensitivity from 93.3% to 100%, specificity from 96.5% to 100%, and F1-scores from 92.8% to 100%. These indicators confirm that all models delivered highly successful classification performance, establishing sufficient reliability for clinical application. The training times for model construction ordered from fastest to slowest were bagging (4.3 s), TotalBoost (9.7 s), LPBoost (46 s), and AdaBoost (536.6 s). Consequently, considering both computational efficiency and classification accuracy, bagging emerged as the optimal model.

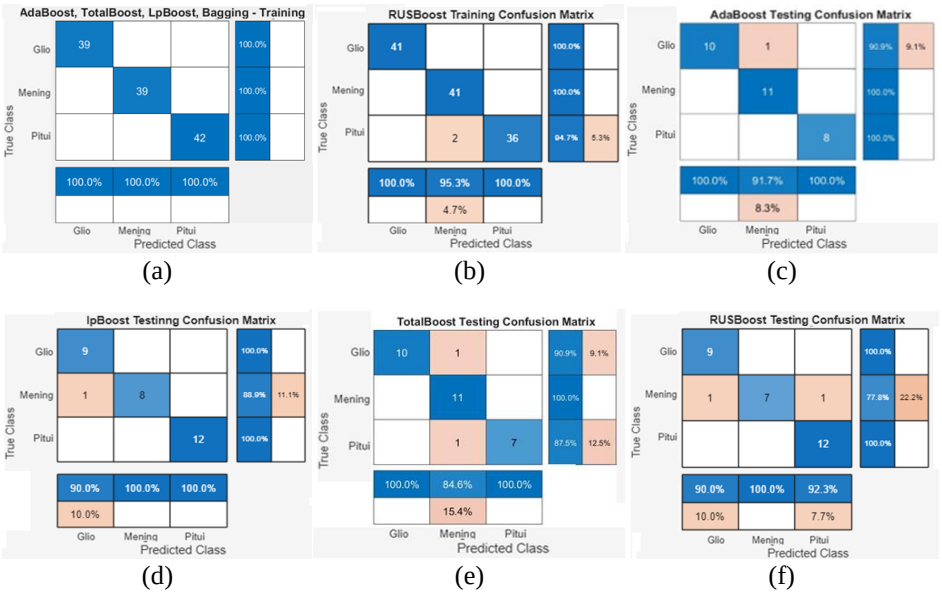

Figure 7. Confusion matrix of five models in case study II; (a) the confusion matrix for the training set of four models: AdaBoost, TotalBoost, LpBoost, and bagging models (100% accuracy), (b) the confusion matrix for the training set of RUSSBoost model 98.3% accuracy), (c) the test set confusion matrix of AdaBoost model (96.7% accuracy), (d) the test set confusion matrix of LPBoost model (96.7% accuracy), (e) the test set confusion matrix of TotalBoost (93.3% accuracy), and (f) the test set confusion matrix of RUSBoost model (93.3% accuracy)

3.2.2. Comparison

Comparison with state-of-art methods: Table 2 compares performance metrics of various approaches in classifying three types of brain tumors on the same dataset. Ismael *et al*. [43] achieved 91.9% accuracy using multilayer perceptrons (MLPs) with statistical features; while Anaraki *et al*. [44] reported 94.2% accuracy with a CNN model using genetic algorithm (GA) and bagging. Sajjad *et al*. [45] used transfer learning to fine-tune VGG19 yielded 90.7%, and Das *et al*. [46]. achieved 94.4% with a CNN featuring 3 convolutional layers and 2 subsampling layers. Sultan *et al*. [47] used 16-layer CNN to achieve 96.1%, Badža and Barjaktarovi [48] used 6 CNN models to achieve from 90% to 97.4% accuracy. Polat and Güngen [49] applied transfer learning to four pretrained models, achieving accuracies between 97.5% and 99.02%, with ResNet50 providing the highest accuracy. The proposed method demonstrated superior performance over reference methods, achieving accuracy between 93.3% and 100% across nine models, as well as other performance metrics also yielded positive results, indicating its promise as a reliable tool for brain tumor classification.

Comparison with existing 2D-EMD approaches: studies using BEMD for MRI image classification remain limited. Therefore, we evaluate our results against three relevant studies. Sahu *et al.* [14] used BEMD to extract first to third-order Autoregressive (AR) coefficients from $BIMF_1$ to $BIMF_4$, producing three feature vectors for SVM classification. Tested on 98 MRI images (33 normal, 65 tumor), their binary SVM with a radial basis function (RBF) kernel achieved 100% accuracy. This superior performance likely stems from their use of mid-level AR coefficients, whereas we leveraged high-level VGG19 features. However, AR coefficients offer greater descriptive compactness. Conversely, Deb *et al.* [15] used BEMD residues (1, 2, and 3) alongside four DL models to classify endoscopic images from the Kvasir dataset. While the residues captured macroscopic shapes and background lighting, the 94.16% accuracy of their squeeze-and-excitation ResNet50 (SE-ResNet50) was lower than our approach. This deficit may be attributed to data blurring in the residue images, whereas our methodology preserves and enhances original image features. Finally, Ghazi *et al.* [16] decomposed mammograms using BEMD to generate five BIMFs, from which they extracted multifractal features. They evaluated 260 images (130 normal and 130 cancerous) from the RCRHKM database in Morocco using an SVM classifier. Their model achieved accuracies ranging from 81.06% to 97.32% across $BIMF_5$ to $BIMF_1$, which are less effective than our proposed approach. Our framework surpasses current state-of-the-art methods in quantitative evaluations, driven by a novel strategy: extracting robust features by the summation of BIMFs and the original images, followed by the integration of multiple classifiers via ensemble learning.

Table 2. Performance comparison with state-of-art-methods using the same dataset

Reference	Data division	Method	N. of models	Acc	Pre	Sen	Spec.	F1
Ismael *et al*. [43]	70/00/30	MLPs	1	91.9	✓	91.1	95.9	✓
Anaraki *et al*.[44]	80/00/20	CNN+GA+Bag	1	94.2	94.3	94.2	97.1	✓
Sajjad *et al*. [45]	50/25/25	Fine-tune VGG19	1	90.7		88.4	96.1	✓
Das *et al*. [46]	66.9/ 16.7/16.3	CNN	1	94.4	93.3	93.0	✓	✓
Sultan *et al*. [47]	60/32/both	CNN	1	96.1	96.1	94.4	✓	✓
Badža and Barjaktarovi [48]	60/20/20	CNN	6 (90% ~ 97.4%)	97.4[1]	97.2[1]	97.8[1]	✓	97.5[1]
Polat and Güngen [49]	70/00/30	Transfer Learning (ResNet50[1])	4 (97.5~99.02%)	99.02[1]	✓	✓	✓	✓
Propose Apr., 2026.	80/0/20	Vgg19 and Ensemble learning	Training set (130 instances)					
			8	100	100`	100	8	100
			1	98.3	98.4[1]	98.4[1]	1	98.4[1]
			Test set (30 instances)					
			1	100	100	100	1	100
			3	96.7	97.0[1]	98.0[1]	3	97.3[1]
			5	93.3	94.7[1]	94.2[1]	5	94.2[1]

Notes:
The proposed approach: 150 images using images and their BIMFs.
Other authors: 3064 images using augmented data.
Data division: training/validation/test.
[1]The best result

3.3. Discussion

Brain MRI segmentation often relies on multilevel thresholding; however, determining the optimal threshold values to accurately detect tumors typically requires iterative trial-and-error. To overcome this, we introduce an enhancement pipeline comprising BEMD, ADF filtering, and morphological contrast enhancement. This pipeline transforms the MRI into an enhanced version with a low-noise histogram, which is then mapped to a $PMF(k)$. While conventional methods apply EMD directly to $PMF(k)$ summing mid-level IMFs to determine the threshold this approach often produces a graph lacking a distinct bimodal shape [8], limiting its use in multi-level thresholding [9]. In this study, we propose smoothing $PMF(k)$ with EWT prior to EMD processing. The resulting hybrid EWT-EMD produces an IMF_1 with a clear, bimodal curve and two distinct peaks. This makes it highly suitable for thresholding without predefined criteria and adaptable for multi-level thresholding via its detrended version. Using EWT to smooth $PMF(k)$ and applying IMF_1 to construct the thresholding curve is a primary contribution of this study. Based on visual and quantitative assessments across nine images, the proposed method yields performance comparable to three conventional multi-level segmentation techniques and one state-of-art.

VGG19 and ensemble learning were used to develop multi-class models for classifying meningioma, glioma, and pituitary tumors by extracting high-level features from ROI images, as well as the sum of ROI images and their ROI of BIMFs via BEMD. BEMD decomposes images into various spatial frequencies. $BIMF_1$ contains the finest details but is discarded because it introduces heavy high-frequency noise. Instead, $BIMF_2$ and $BIMF_3$ which detect medium-scale textures are added back to the image. They amplify subtle, informative details to enhance features without amplifying noise. Consequently, the extracted features retain significant details that are capable of differentiating the morphology of different tumor types. Higher-order BIMFs are also discarded, as they only reveal coarse background structures that are irrelevant for classification [16]. The results demonstrate that features derived from combined ROI images and ROI of $BIMF_2$ and $BIMF_3$ generate better models than using standalone ROI image features and are also more accurate. In addition to high accuracy, the models obtained in this study have high sensitivity values, minimizing misclassification a crucial aspect of medical diagnosis thereby confirming the reliability of the proposed method. This is another key contribution of the proposed approach.

4. CONCLUSION

The proposed method proposes an analytical framework for a CADx system that uses EMD and BEMD two adaptive decomposition methods. The approach focuses on the final two stages of the process and was evaluated on clinical MRI scans from the Figshare brain tumor dataset. Tumor segmentation on a subset of nine images demonstrated complete visual agreement between the detected tumors and the ground-truth masks. Quantitative results demonstrated a high average precision of 96.70%, a sensitivity of 91.07%, and an F1-score of 93.70. These high metrics indicated that the model effectively minimized false positives

and false negatives, ensuring a balanced equilibrium between detected tumors and ground truths. By accurately identifying tumor locations and boundaries, this method enabled rapid, reliable tumor identification a critical requirement for effective brain tumor diagnosis. Tumor classification was conducted on 150 MRIs of three brain tumor types, using a 224×224 ROI around the tumors to calculate BEMD components. Feature extraction used VGG19 and divided into two groups: (i) features from ROIs of denoised images, achieving four ensemble models (SubBoost, AdaBoost, LPBoost, and bagging) with 100% training accuracy and test accuracies between 93.3% and 96.7%; and (ii) features from a combination of denoised images and their $BIMF_2$ and $BIMF_3$, leading to five models with four (bagging, AdaBoost, LPBoost, and TotalBoost) achieving 100% training accuracy, and one (RUSBoost) reached 98.3%. For testing, bagging achieved 100% accuracy, with others ranging between 93.3% and 96.7%. The results indicate that using features derived from combining denoised images with BEMD components produces models that effectively reduce misclassifications. This approach shows that the models ensure reliable predictions, support precise tumor typing, thereby facilitating targeted therapies that can improve patient survival.

In a clinical setting, manual image interpretation is an intricate task that demands significant time and specialized expertise from radiologists. The results outlined above demonstrate that the EMD/BEMD approach significantly improves the accuracy of both image segmentation and classification, representing a meaningful advancement in the field of medical image analysis. Furthermore, implementing our proposed method as a CADx system provides objective, repeatable, and justifiable outcomes. This approach reliably supports physicians in reducing diagnostic turnaround times and improving overall accuracy, which ultimately enables more timely treatment decisions.

Despite these advancements, the proposed method faces several limitations. Notably, the restricted dataset limits tumor diversity, while reliance on T1-weighted modality data hinders broader generalizability. Furthermore, using VGG19 solely for feature extraction fails to fully exploit its capabilities. Crucially, the lack of integration between the algorithm's outputs and clinical perspectives, compounded by slow computation speeds, restricts its practical utility and real-time diagnostic potential. Future work will address these constraints by incorporating larger, more diverse datasets, using multimodal imaging, and optimizing both computational speed and classification algorithms. This effort will yield a comprehensive CADx tool featuring cloud connectivity for remote clinical diagnostics. To validate these applications, the software will be deployed in clinical settings through collaborative partnerships with physicians at university-affiliated hospitals.

FUNDING INFORMATION

No financial support from any organizations.

AUTHOR CONTRIBUTIONS STATEMENT

This journal uses the Contributor Roles Taxonomy (CRediT) to recognize individual author contributions, reduce authorship disputes, and facilitate collaboration.

Name of Author	C	M	So	Va	Fo	I	R	D	O	E	Vi	Su	P	Fu
Giang Hong Nguyen	✓	✓	✓	✓	✓	✓	✓	✓	✓	✓	✓		✓	
Yen Thi Hoang Hua			✓							✓	✓			
Ngan Vuong Thuy Nguyen			✓							✓	✓			
Liet Van Dang	✓	✓								✓	✓	✓	✓	

C : **C**onceptualization
M : **M**ethodology
So : **So**ftware
Va : **Va**lidation
Fo : **Fo**rmal analysis
I : **I**nvestigation
R : **R**esources
D : **D**ata Curation
O : Writing - **O**riginal Draft
E : Writing - Review & **E**diting
Vi : **Vi**sualization
Su : **Su**pervision
P : **P**roject administration
Fu : **Fu**nding acquisition

CONFLICT OF INTEREST STATEMENT

Authors state no conflict of interest.

DATA AVAILABILITY

The data used in this article was downloaded from Jun Cheng's Figshare Publicity Brain dataset 2015 (https://figshare.com/articles/dataset/brain_tumor_dataset/1512427).

REFERENCES

[1] S. Kim *et al.*, "Global burden of brain and central nervous system cancer in 185 countries, and projections up to 2050: a population-based systematic analysis of GLOBOCAN 2022," *Journal of neuro-oncology*, vol. 175, no. 2, pp. 673–685, Nov. 2025, doi: 10.1007/S11060-025-05164-0.

[2] M. F. Almufareh, M. Imran, A. Khan, M. Humayun, and M. Asim, "Automated brain tumor segmentation and classification in MRI using YOLO-based deep learning," *IEEE Access*, vol. 12, pp. 16189–16207, 2024, doi: 10.1109/ACCESS.2024.3359418.

[3] T. A. Fahim, F. B. Alam, and M. A. Hossain, "Brain tumor detection, classification and segmentation by deep learning models from MRI images: Recent approaches, challenges and future directions," *Array*, vol. 28, p. 100571, Dec. 2025, doi: 10.1016/j.array.2025.100571.

[4] M. A. Bamaleibd and U. Alqasemi, "Computer-aided detection system of MRI brain tumor images," *Journal of King Abdulaziz University: Engineering Sciences*, vol. 33, no. 2, pp. 19–33, Dec. 2023, doi: 10.4197/ENG.33-2.2.

[5] T. H. Shemanto, L. B. Billah, and M. A. Ibtesham, "A novel method of thresholding for brain tumor segmentation and detection," *Studies in Autonomic, Data-driven and Industrial Computing*, pp. 277–289, 2023, doi: 10.1007/978-981-19-7528-8_22.

[6] S. R. Sharma, S. Alshathri, B. Singh, M. Kaur, R. R. Mostafa, and W. El-Shafai, "Hybrid multilevel thresholding image segmentation approach for brain MRI," *Diagnostics 2023, Vol. 13, Page 925*, vol. 13, no. 5, p. 925, Mar. 2023, doi: 10.3390/DIAGNOSTICS13050925.

[7] T. Akan, A. G. Oskouei, S. Alp, and M. A. N. Bhuiyan, "Brain magnetic resonance image (MRI) segmentation using multimodal optimization," *Multimedia Tools and Applications 2024 84:16*, vol. 84, no. 16, pp. 16971–17020, Jul. 2024, doi: 10.1007/S11042-024-19725-4.

[8] S. Krinidis, M. Krinidis, and V. Chatzis, "An empirical method for threshold selection," *International Journal of Signal Processing. Image Processing and Pattern Recognition*, vol. 5, no. 2, pp. 101–114, Jun. 2012.

[9] B. S. Rao and E. S. Reddy, "EMD based fuzzy C-means clustering algorithm for medical image segmentation," *International Journal of Applied Engineering Research*, vol. 10, no. 20, pp. 41400–41405, 2015. [Online]. Available: https://www.ripublication.com/ijaer10/ijaerv10n20_106.pdf

[10] K. Lakshmi, S. Amaran, G. Subbulakshmi, S. Padmini, G. P. Joshi, and W. Cho, "Explainable artificial intelligence with UNet based segmentation and Bayesian machine learning for classification of brain tumors using MRI images," *Scientific Reports 2025*, vol. 15, no. 1, pp. 690–712, Jan. 2025, doi: 10.1038/s41598-024-84692-7.

[11] M. Aamir, Z. Rahman, U. A. Bhatti, W. A. Abro, J. A. Bhutto, and Z. He, "An automated deep learning framework for brain tumor classification using MRI imagery," *Scientific Reports 2025*, vol. 15, no. 1, pp. 17593–17615, May 2025, doi: 10.1038/s41598-025-02209-2.

[12] P. R. Kumar *et al.*, "A novel brain MRI classification framework integrating tuned single scale retinex and empirical wavelet entropy features," *Scientific Reports 2025*, vol. 15, no. 1, pp. 29765–29781, Aug. 2025, doi: 10.1038/s41598-025-13281-z.

[13] A. Gudigar, U. Raghavendra, E. J. Ciaccio, N. Arunkumar, E. Abdulhay, and U. R. Acharya, "Automated categorization of multi-class brain abnormalities using decomposition techniques with MRI images: A comparative study," *IEEE Access*, vol. 7, pp. 28498–28509, 2019, doi: 10.1109/ACCESS.2019.2901055.

[14] O. Sahu, V. Anand, V. Kanhangad, and R. B. Pachori, "Classification of magnetic resonance brain images using bi-dimensional empirical mode decomposition and autoregressive model," *Biomedical Engineering Letters*, vol. 5, no. 4, pp. 311–320, Dec. 2015, doi: 10.1007/S13534-015-0208-9.

[15] M. Deb *et al.*, "Empirical mode decomposition-based deep learning model development for medical imaging: feasibility study for gastrointestinal endoscopic image classification," *Journal of Imaging 2026*, vol. 12, no. 1, p. 23, Dec. 2025, doi: 10.3390/JIMAGING12010004.

[16] F. Ghazi, K. Ibrahimi, F. Ayoub, A. Benkuider, and M. Zraidi, "Classification of mammography images based on multifractal analysis of BIMFs," *International journal of biomedical imaging*, vol. 2025, no. 1, p. 30, Dec. 2025, doi: 10.1155/IJBI/5940783.

[17] Jun Cheng, "Figshare - brain tumor dataset," Apr. 2017.

[18] Jun Cheng *et al.*, "Correction: enhanced performance of brain tumor classification via tumor region augmentation and partition," *PLOS ONE*, vol. 10, no. 12, p. e0144479, Dec. 2015, doi: 10.1371/JOURNAL.PONE.0144479.

[19] M. Thirumalaisamy, "Fast and adaptive multivariate and multidimensional EMD," *File Exchange - MATLAB Central*, May 2019.

[20] D. Lopes, "Anisotropic diffusion (Perona & Malik)," *File Exchange - MATLAB Central*, May 2007.

[21] I. Rakhmatulin, "Encoder with the empirical mode decomposition (EMD) to remove muscle artefacts from EEG signal," *arXiv*, Sep. 2024.

[22] J. Gilles, "Empirical wavelet transform," *IEEE Transactions on Signal Processing*, vol. 61, no. 16, pp. 3999–4010, 2013, doi: 10.1109/TSP.2013.2265222.

[23] Y. Xia, B. Zhang, W. Pei, and D. P. Mandic, "Bidimensional multivariate empirical mode decomposition with applications in multi-scale image fusion," *IEEE Access*, vol. 7, pp. 114261–114270, 2019, doi: 10.1109/ACCESS.2019.2936030.

[24] "How to perform skull stripping using matlab?," *MATLAB Answers - MATLAB Central*, May 2021.

[25] G. Nguyen, Y. Hua, L. Nguyen, and L. Dang, "Image enhancement using bidimensional empirical mode decomposition and morphological operations for brain tumor detection and classification," *Asian Pacific journal of cancer prevention : APJCP*, vol. 25, no. 9, pp. 3327–3336, 2024, doi: 10.31557/APJCP.2024.25.9.3327.

[26] J. Kang, Z. Ullah, and J. Gwak, "Mri-based brain tumor classification using ensemble of deep features and machine learning classifiers," *Sensors*, vol. 21, no. 6, pp. 1–21, Mar. 2021, doi: 10.3390/s21062222.

[27] B. Qawasmeh, J. S. Oh, and V. Kwigizile, "Comparative analysis of alexNet, resNet-50, and VGG-19 performance for automated feature recognition in pedestrian crash diagrams," *Applied Sciences (Switzerland)*, vol. 15, no. 6, p. 27, Mar. 2025, doi: 10.3390/app15062928.

[28] H. Jafarzadeh, M. Mahdianpari, E. Gill, F. Mohammadimanesh, and S. Homayouni, "Bagging and boosting ensemble classifiers for classification of multispectral, hyperspectral and polSAR data: A comparative evaluation," *Remote Sensing*, vol. 13, no. 21, p. 22, Nov. 2021, doi: 10.3390/rs13214405.

[29] K. M. Sujon, R. Hassan, K. Choi, and M. A. Samad, "Accuracy, precision, recall, f1-score, or MCC? empirical evidence from

advanced statistics, ML, and XAI for evaluating business predictive models," *Journal of Big Data 2025*, vol. 12, no. 1, p. 45, Dec. 2025, doi: 10.1186/S40537-025-01313-4.
[30] "Multithresh - multilevel image thresholds using Otsu's method," *MATLAB Central*. [Online]. Available: https://www.mathworks.com/help/images/ref/multithresh.html
[31] D. Oliva, "Multilevel thresholding segmentation based on harmony search optimization -file exchange - MATLAB Central," *File Exchange - MATLAB Central*, Jun. 2014.
[32] A. Dixit, "Fast kmeans algorithm code," *File Exchange - MATLAB Central*.
[33] S. Dhodle and S. Miriala, "Brain tumor segmentation and classification using machine learning with feature selection," *Franklin Open*, vol. 16, p. 100689, Sep. 2026, doi: 10.1016/j.fraope.2026.100689.
[34] N. H. Giang, H. T. H. Yen, N. C. Linh, and L. V. Dang, "MRI brain image denoising and tumor detection using 1-D and 2-D empirical mode decomposition," *International Journal of Advanced Technology and Engineering Exploration*, vol. 13, no. 134, pp. 102–122, Jan. 2026, doi: 10.19101/IJATEE.2025.121220203.
[35] "Fitcensemble - Fit ensemble of learners for classification," *MATLAB Central*. [Online]. Available: https://www.mathworks.com/help/stats/fitcensemble.html
[36] C. Staerk and A. Mayr, "Randomized boosting with multivariable base-learners for high-dimensional variable selection and prediction," *BMC bioinformatics*, vol. 22, no. 1, pp. 1–28, Dec. 2021, doi: 10.1186/S12859-021-04340-Z.
[37] H. Zhao, W. Liu, Y. Wang, and L. Wu, "Comparative analysis of algorithmic approaches in ensemble learning: bagging vs. boosting," *Scientific reports*, vol. 15, no. 1, p. 12, Oct. 2025, doi: 10.1038/S41598-025-15971-0.
[38] "Decision trees," *Scikit-learn developers*.
[39] M. Azad, T. H. Nehal, and M. Moshkov, "A novel ensemble learning method using majority based voting of multiple selective decision trees," *Computing*, vol. 107, no. 42, p. 33, Jan. 2025, doi: 10.1007/S00607-024-01394-8.
[40] "Surrogate splits," *MATLAB & Simulink*.
[41] "LPBoost and totalBoost for small ensembles," *MATLAB & Simulink*.
[42] C. Seiffert, T. M. Khoshgoftaar, J. Van Hulse, and A. Napolitano, "RUSBoost: a hybrid approach to alleviating class imbalance," *IEEE Transactions on Systems, Man, and Cybernetics Part A:Systems and Humans*, vol. 40, no. 1, pp. 185–197, Jan. 2010, doi: 10.1109/TSMCA.2009.2029559.
[43] M. R. Ismael and I. Abdel-Qader, "Brain tumor classification via statistical features and back-propagation neural network," *IEEE International Conference on Electro Information Technology*, vol. 2018-May, pp. 252–257, Oct. 2018, doi: 10.1109/EIT.2018.8500308.
[44] A. K. Anaraki, M. Ayati, and F. Kazemi, "Magnetic resonance imaging-based brain tumor grades classification and grading via convolutional neural networks and genetic algorithms," *Biocybernetics and Biomedical Engineering*, vol. 39, no. 1, pp. 63–74, Jan. 2019, doi: 10.1016/J.BBE.2018.10.004.
[45] M. Sajjad, S. Khan, K. Muhammad, W. Wu, A. Ullah, and S. W. Baik, "Multi-grade brain tumor classification using deep CNN with extensive data augmentation," *Journal of Computational Science*, vol. 30, pp. 174–182, Jan. 2019, doi: 10.1016/J.JOCS.2018.12.003.
[46] S. Das, O. R. R. Aranya, and N. N. Labiba, "Brain tumor classification using convolutional neural network," *1st International Conference on Advances in Science, Engineering and Robotics Technology 2019 (ICASERT 2019)*, p. 5, May 2019, doi: 10.1109/ICASERT.2019.8934603.
[47] H. H. Sultan, N. M. Salem, and W. Al-Atabany, "Multi-classification of brain tumor images using deep neural network," *IEEE Access*, vol. 7, pp. 69215–69225, 2019, doi: 10.1109/ACCESS.2019.2919122.
[48] M. M. Badža and M. C. Barjaktarović, "Classification of brain tumors from MRI images using a convolutional neural network," *Applied Sciences 2020*, vol. 10, no. 6, p. 13, Mar. 2020, doi: 10.3390/APP10061999.
[49] Ö. Polat and C. Güngen, "Classification of brain tumors from MR images using deep transfer learning," *The Journal of Supercomputing 2021*, vol. 77, no. 7, pp. 7236–7252, Jan. 2021, doi: 10.1007/S11227-020-03572-9.

BIOGRAPHIES OF AUTHORS

Giang Hong Nguyen received the B.Sc. degree in Physics from the University of Science, Ho Chi Minh City, Vietnam, in 2009, and the M.Sc. degree in Physics and Physics Engineering from the University of Science, Vietnam National University Ho Chi Minh City, Vietnam, in 2021. He is currently a lecturer with the Faculty of General Education, Cao Thang Technical College, Sai Gon Ward, Ho Chi Minh City, Vietnam. He is also currently pursuing the Ph.D. degree with the Department of Physics and Computer Science, Faculty of Physics and Engineering Physics, University of Science, Vietnam National University Ho Chi Minh City, Vietnam. His research interests include medical image processing, image analysis, machine learning, deep learning, computer vision, and brain magnetic resonance imaging (MRI). He can be contacted at email: nguyenhonggiang@caothang.edu.vn, 22n38101@student.hcmus.edu.vn.

Yen Thi Hoang Hua received the B.Sc. degree in Physics from the University of Science, Vietnam National University Ho Chi Minh City, Vietnam, in 2005, and the M.Sc. degree in Physics and Electrical Engineering from the University of Science, Vietnam National University Ho Chi Minh City, Vietnam, in 2007. She is currently a lecturer with the Department of Physics and Computer Science, Faculty of Physics and Engineering Physics, University of Science, Vietnam National University Ho Chi Minh City, Vietnam. Her research interests include digital signal processing, image processing, machine learning, and deep learning. She can be contacted at email: hthyen@hcmus.edu.vn.

Ngan Vuong Thuy Nguyen received the M.Sc. degree in Radio Electronics Physics from Vietnam National University Ho Chi Minh City, Vietnam, in 2019, and a second M.S. degree in Computer Science from Texas Tech University, Lubbock, TX, USA, in 2023. She is currently a lecturer with the Faculty of Physics and Engineering Physics, University of Science, Vietnam National University Ho Chi Minh City, Vietnam. Her research interests include signal processing, active noise control, data visualization, big data analytics, medical image processing, and magnetic resonance imaging (MRI) image enhancement. She has authored and co-authored more than 30 publications in international journals and conference proceedings, including IEEE Big Data, IEEE COMPSAC, and the International Symposium on Visual Computing. She is currently the Principal Investigator of a Vietnam National University Ho Chi Minh City-funded research project on brain MRI image enhancement and tumor segmentation. She can be contacted at email: nvtngan@hcmus.edu.vn, nguyenvuongthuyngan@gmail.com.

Liet Van Dang received the Ph.D. degree in Mathematics and Physics from the University of Ho Chi Minh City (now Vietnam National University Ho Chi Minh City, Vietnam) in 1995. He is currently an Associate Professor with the Department of Nature, Dong Nai University, Tam Hiep Ward, Dong Nai City, Vietnam. His research interests include signal processing, image processing, machine learning, and gravity and magnetic data interpretation. He can be contacted at email: dangvanliet@gmail.com.